# Search for Dark Matter in the halo of Milky Way via microlensing

Arash Mirhosseini
Université Paris-sud

Supervisor: Dr. Marc Moniez
Laboratoire de l'Accélérateur Linéaire, CNRS

June 2017

# Contents

# 1 Introduction

Over the last three decades, it has generally been accepted that most of the matter contents in the Universe are in the form of dark matter. Since the dark matter does not interact electromagnetically, its detection has been always a hard task. One useful method to probe the amount of dark matter is to measure the bending of light rays of luminous objects when they pass through the gravitational field of dark matter. If the deflectors are sub-stellar or stellar-mass objects, this technique is called *microlensing*.

During 1990s several collaborations started to use the microlensing in order to estimate the amount of dark matter in the form of compact massive object in the halo of Milky Way. The EROS and MACHO collaborations monitored the brightness of millions of stars in the Magellanic Clouds for several years to detect possible microlensing events, and they reported several candidates (Alcock et al. (1997); Ansari et al. (1996)) with a timescale between 33 days to 266 days. Taken together, their results were widely seen as ruling out any significant component of dark matter in the form of compact bodies with a mass range between $10^{-7}M_{\odot}$ to $1M_{\odot}$.

The sensitivity of a microlensing experiment is determined by various parameters. For the past and current experiments the microlensing events of very low-mass objects ($M < 10^{-7}M_{\odot}$) were too short to be detected by the experiments. Furthermore, massive objects with a few tens of solar masses have long duration events and they could not be detected as well. So the sensitivity of these experiments were between $10^{-7}M_{\odot}$ to $1M_{\odot}$. Figure 1 shows the limit set on the massive compact objects of Galactic halo by EROS experiment. From this figure it is clear that the compact objects in the range of $10^{-7}M_{\odot}$ to $1M_{\odot}$ cannot contribute to more than 10% of dark halo.

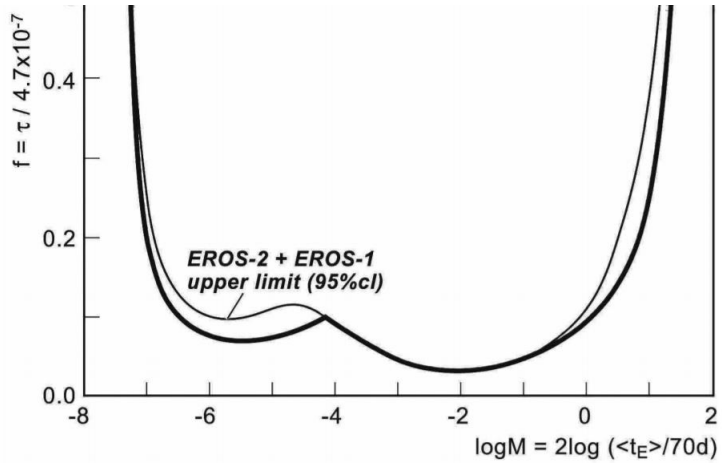


Figure 1: Exclusion diagram at 95% C.L. for the standard halo model. The thick line shows the combined EROS + MACHO 95% C.L. upper limit on $f = \tau_{LMC}/4 \times 10^{-7}$ based on no observed events. The thin line is the EROS limit (Moniez (2010))

The recent discovery of gravitational waves (that were produced by a system of binary black holes of a few solar masses) could be a hint of existence of such compact and very massive objects ($> 10M_{\odot}$) in the halo of our Galaxy. If they exist, it should be possible to detect the microlensing events that are produced by these objects. Since the timescale of a microlensing event increases with the mass of the lens (see section 2.2), longer observations can help us to detect more massive objects in the halo of our Galaxy. The main goal of this internship is to test the combination of the data of microlensing experiments (particularly EROS 1 plate and MACHO surveys) to find new and long duration microlensing events of massive object with a few tens of solar masses or more.

The next two sections of this report (sections 2 and 3) give an overview of the microlensing phenomenon, and of the EROS analysis. In the section 4, I estimate the common field of view between different surveys and using a reasonable hypothesis I generate the efficiency for longer observations. Then I compute the event rate and the expected number of events for three different masses. In sections 5 and 6, I explain EROS 1 plate and MACHO surveys and I devise an algorithm to find the counterpart of an EROS 1 plate object survey in MACHO database. In section 6, I try to construct the joint light curves of objects in different surveys.

# 2 Basic definitions

## 2.1 Geometry of microlensing phenomenon

Figure 2 shows the principle of gravitational microlensing. Let us consider a source star at a distance $D_s$ from the observer, and a lens deflector at a distance $D_d$ from the observer and $D_{ds}$ from the source. According to General relativity, the lens situated between the observer and the source deflects the source's light by an angle $\theta$:

$$\theta = \frac{4G\pi}{c^2} \times \frac{1}{r}, \tag{1}$$

where $G$ is the gravitational constant, $M$ the mass of the lens, $c$ speed of light and $r$ the distance from the lens to the undeflected light ray.

Because of the deflection of light two separate images are produced. If $b$ is the impact parameter (i.e. the perpendicular distance of the lens to the line joining the source and the observer), the following equation can be obtained:

$$r - b = \frac{4GM}{rc^2}\frac{D_d D_{ds}}{D_s}. \tag{2}$$

In particular, when observer, lens and source are perfectly aligned ($b = 0$), the image of the source becomes a ring and the radius of the ring in the plane of the lens is called Einstein radius $R_E$. Hence, one can find the Einstein radius by putting $b = 0$ (that is the case of Einstein ring formation) in Eq. 2 and solve it for $r$:

$$R_E = \sqrt{\frac{4GM}{c^2}\frac{D_d D_{ds}}{D_s}} = \sqrt{\frac{4GM}{c^2} D_s x(1-x)}, \tag{3}$$

where $x \equiv D_d/D_s$ gives the fraction of distance between the lens-observer and source-observer. Now, Eq. 2 can be re-written in terms of Einstein radius:

$$r_{1,2} = 1/2\Big(b \pm \sqrt{b^2 + 4R_E^2}\Big), \tag{4}$$

where $r_{1,2}$ correspond to the two light rays that form two separate images.

In the microlensing situation, the mass of the lens is of the order of solar mass. In this case the angular separation between multiple images of a source is very small, so that they cannot be resolved and multiple images are recorded as a single image with an increase in apparent brightness of the image. The standard light curve of a microlensing event is shown in the figure 3

## 2.2 Timescale of microlensing event

The lens which is inside the halo of Milky Way has a relative velocity with respect to the line of sight. As a result the light intensity of the source is first increased as it gets closer to the lens, then decreased as the deflector moves

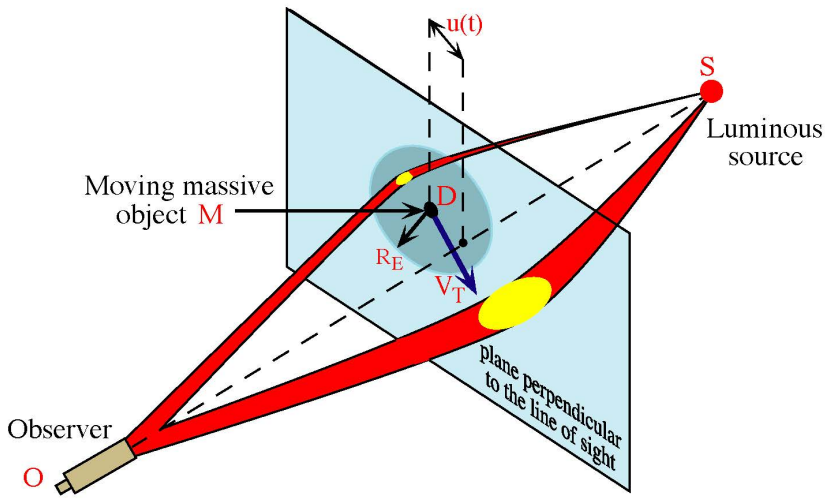


Figure 2: Principle of the microlensing effect. The lens $D$ of mass $M$ moves with a transverse relative speed $v_T$ with respect to the line of sight $OS$. Therefore the impact parameter $u(t)$ (in unit of Einstein Radius $R_E$) changes with time, and so does the magnification of the source.

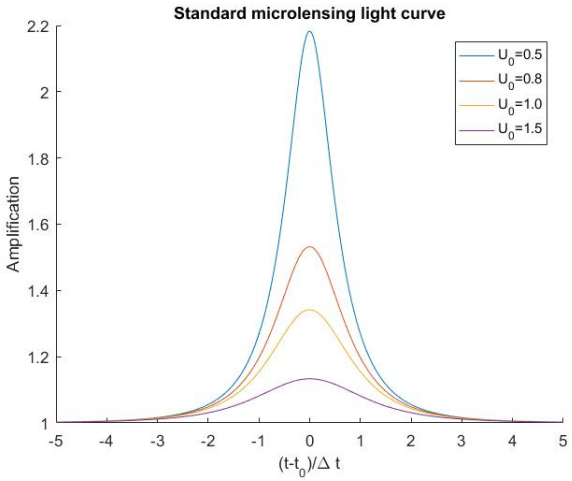


Figure 3: Time dependence of magnification during a microlensing event. When the minimum distance between the lens and the source ($u_0$) increases, the microlensing effect becomes less and less effective.

away. If $v_T$ is the relative transverse velocity of the source, the time dependence of the distance from the lens can be expressed as:

$$u(t) = \sqrt{u_0^2 + \frac{v_t^2(t-t_0)^2}{R_E^2}}, \tag{5}$$

where $t_0$ is the instant at which the projection of the source in the plane of the lens is closest to the lens, and $u_0$ is the impact parameter at $t = t_0$ (see figure 2).

The timescale $t_E$ of the microlensing event is defined as the time it takes for the source to move by one Einstein radius:

$$t_E \equiv \frac{R_E}{v_t} = \frac{1}{v_t} \times \sqrt{\frac{4GM}{c^2} D_s x(1-x)}, \tag{6}$$

or (in days):

$$t_E \approx 79 \Big[\frac{100\text{km/s}}{v_t}\Big] \Big[\frac{M}{M_\odot}\Big]^{\frac{1}{2}} \Big[\frac{D_s}{10\text{k}pc}\Big]^{\frac{1}{2}} \frac{\sqrt{x(1-x)}}{0.5} \tag{7}$$

# 3 Summary of EROS2 analysis

In this section, I use a simple model to compute the timescale and detection probability of microlensing events at a given time.

Eq. 7 shows that the timescale of a microlensing event is directly proportional to the square root of mass $M$. The only observable in Eq. 7 is the time scale of microlensing event $t_E$, and the three parameters $M$, $v_T$ and $x$ are randomly distributed variables. The 3-fold degeneracy in Eq. 7 makes the interpretation of microlensing results difficult. In the following, the random relative transverse velocities are generated according to the Maxwellian distribution of velocities, and random distances $x$ are generated according to the standard halo model, and for three given masses $M = 10M_\odot, M = 100M_\odot$ and $M = 1000M_\odot$ the timescales are computed.

## 3.1 Halo model

To simulate the distribution of distance variable ($x$), I use the simplest halo density model which is spherical, isothermal and isotropic. This model generates the flat rotation curve observed for spiral galaxies, and the mass distribution is given by:

$$\rho(r) = \rho_0 \frac{a^2 + r_\odot^2}{a^2 + r^2}, \tag{8}$$

where $\rho_0 \approx 7.9 \times 10^{-3} M_\odot \text{pc}^{-3}$ is the local dark matter density, $a \approx 3$ Kpc is the Galaxy core radius and $r_\odot = 8.5$ kpc is the distance from the Sun to the center of the Galaxy. Since distance $r$ is measured in galactocentric coordinates, it is the distance of halo objects to the Galactic center. But in order to find the density in terms of $x$, we need the

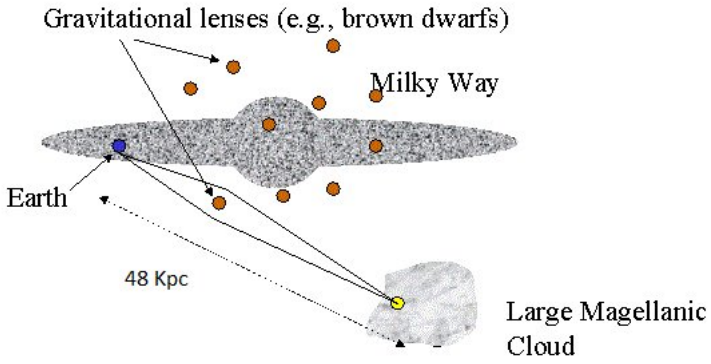


Figure 4: Sketch of the Galaxy, halo objects around the Galaxy, and Large Magellanic Cloud.

distance along our line of sight. So a change of coordinates is needed to convert $r$ to $x$ (distance unit along our line of sight). Using a simple geometrical picture (figure 4), the following change of coordinates can be used:

$$\begin{aligned} x_{lens} &= xD_s \times cos(b)cos(l) \\ y_{lens} &= xD_s \times cos(b)sin(l) \\ z_{lens} &= xD_s \times sin(b) \end{aligned} \tag{9}$$

where $b$ and $l$ are the galactic latitude and galactic longitude of the target, respectively. Since our target is LMC, one must use the galactic coordinates of LMC ($b = -32.89°$, $l = 280.47°$). Substitution of Eqs. 9 and LMC galactic coordinates into Eq. 8 gives the density of halo objects along our line of sight $\rho(x)$:

$$\rho(x) = \rho_0 \frac{a^2 + r_\odot^2}{a^2 + (2303.24x^2 - 124x + 72.25)} \tag{10}$$

The number of lenses along our line of sight per solid angle per unit distance is: $\frac{dN_{lens}}{dxd\Omega} = \frac{(\rho/M)dv}{dxd\Omega} \propto \rho x^2$. Figure 5a shows the distribution of lenses generated according to a random generator with $\frac{dN_{lens}}{dxd\Omega} \propto \rho x^2$.

### 3.2 Transverse velocity distribution of the sources

In the following, I assume that the transverse velocity ($v_T$) distribution of the sources in the Large Magellanic cloud follows a Maxwellian distribution:

$$H(v_T) = \frac{2v_T}{(220\text{km/s})^2} \exp\Big[ - \frac{v_T^2}{(220\text{km/s})^2} \Big] \tag{11}$$

Figure 5b which is produced by generation of random numbers using Monte-Carlo method, shows the distribution of transverse velocities according to Eq. 11.

### 3.3 Timescale and probability of a microlensing event duration

Eq. 7 shows that timescale of a microlensing event is directly proportional to the square root of the mass of the lens. One can use the most probable values of distance $x$ and velocity $v_T$, and the distance to LMC (48 Kpc) to plot the average timescale versus mass of the lens. The result is shown in the figure 6.

For a given mass $M$, there is a degeneracy between $x$ and $v_T$, and different values for these two parameters can lead to an identical timescale $t_E$. From now on I only consider the following three masses: $M = 10M_\odot, M = 100M_\odot$, and $M = 1000M_\odot$. Relative transverse velocities $v_T$ and distances $x$ are generated according to the Eqs. 11 and 10 (by means of Monte-Carlo method). Then one can count the number of microlensing events (at a given time) in each timescale bin. After normalization, the resulting histogram (figure 7) shows the probability that a source is magnified by more than 34% (i.e within one Einstein radius) as a function of $t_E$. As we expect, the mean timescale $t_E$ increases with the square root of the lens mass.

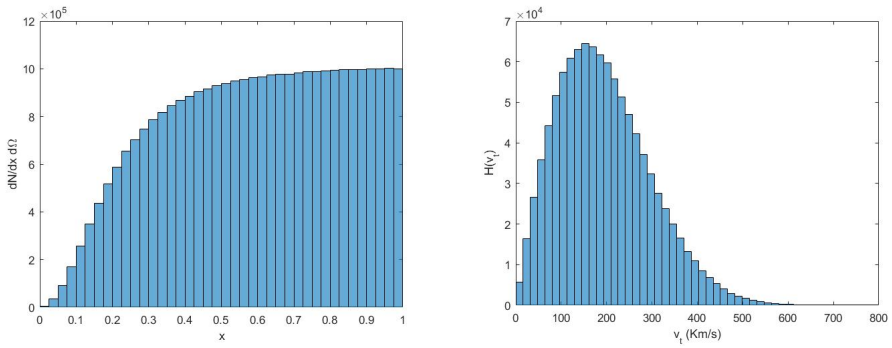


(a) (b)

Figure 5: (a) Distribution of random numbers according to $\frac{dN_{lens}}{dxd\Omega} \propto \rho x^2$. (b) Distribution of random numbers according to Maxwellian distribution of transverse velocity.

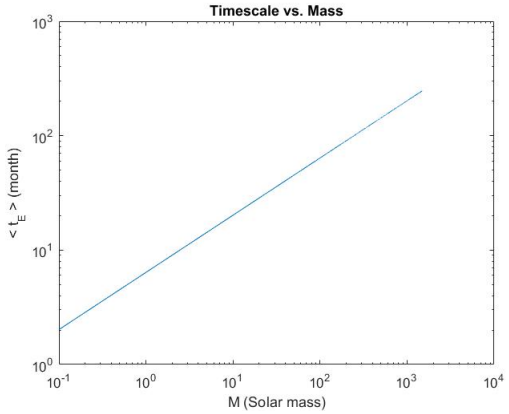


Figure 6: Variation of timescale vs. lens mass for fixed values of $x = 0.6$ and $v_T = 198$ Km/s.

### 3.4 Event rate

The event rate is proportional to the integral of the number of events weighted by $1/t_E$. Hence, as the first step, we would like to have a histogram in which each of the events in the bins has a weight of $1/t_E$. The results for three masses are shown in the figure 8.

The event rate $\Gamma$ can be computed from $N$ events as follows:

$$\Gamma = \frac{2}{\pi} \sum_{i=1}^{N} \frac{N_i}{t_{E_i}} \times \tau, \tag{12}$$

where $N_i$ is the number of events in a bin centered at $t_{E_i}$, $\tau \approx 10^{-6}$ is the optical depth. Optical depth is defined as the probability that at a given time, a given star is inside the Einstein circle (i.e. magnified by more than 34%). The timescale of microlensing events was defined as the time it takes for the source to move by one Einstein radius. However, it is possible that the source is inside the Einstein ring (i.e detected as microlensing event), but it does not move by one Einstein radius. The factor $\frac{2}{\pi}$ is a correction for this effect.

Table 1 shows the event rate for three lenses.

| Mass | $\Gamma$(event yr$^{-1}$ star$^{-1}$) |
|---|---|
| 10 $M_\odot$ | $5.27 \times 10^{-7}$ |
| 100 $M_\odot$ | $1.67 \times 10^{-7}$ |
| 1000 $M_\odot$ | $5.27 \times 10^{-8}$ |

Table 1: Event rate $\Gamma$ for three different masses.

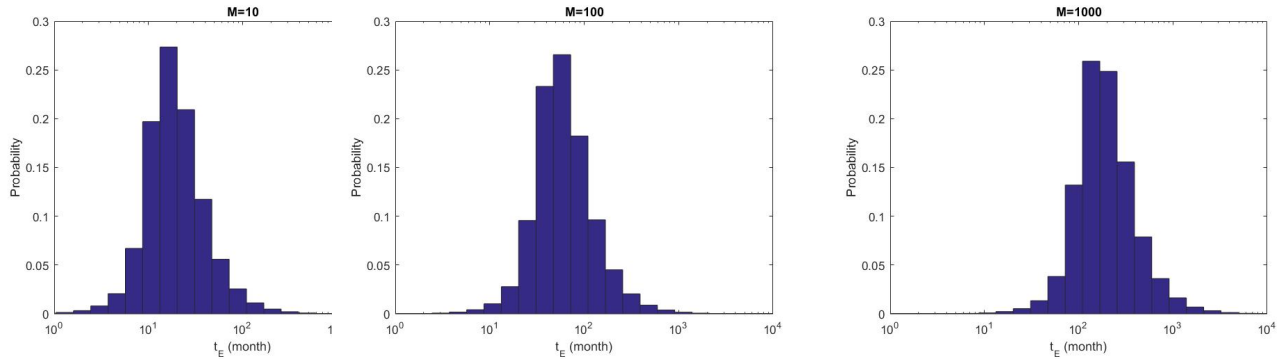


(a) (b) (c)

Figure 7: Distribution of timescale of microlensing events with a timescale $t_E$ for three different masses: $M = 10$, $M = 100$, and $M = 1000$ (a, b, c, respectively) in units of solar mass. The timescale corresponding to the maximum probability increases with increasing mass.

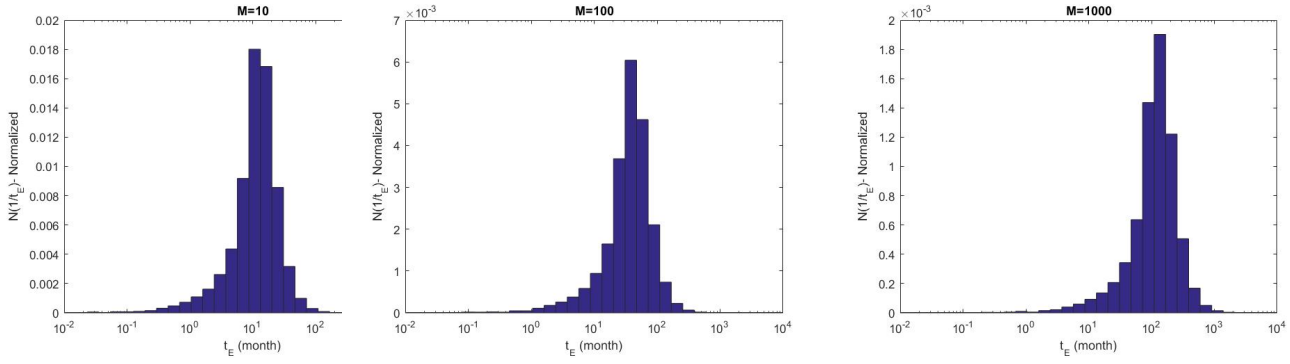


(a) (b) (c)

Figure 8: Rate of events for $M = 10$, $M = 100$, and $M = 1000$ (a, b, c, respectively) in units of solar mass.

### 3.5 Detection efficiency

The detection efficiency of a microlensing survey is defined as the ratio of the number of microlensing events satisfying selection requirement ($N_{obs}$) to the total number of events with $u_0 < 1$. Figure 9 shows the detection efficiency of EROS2 survey towards LMC. In order to introduce the effect of efficiency on the shape of the figures 8a to 8c, the efficiencies for various timescales $t_E$ are interpolated linearly as the first step. The results are shown in the figure **??**a. Multiplying rate by the efficiency values $\epsilon(t_{E_i})$ gives the expected values after taking into account the efficiency. The results are shown in the figure 10

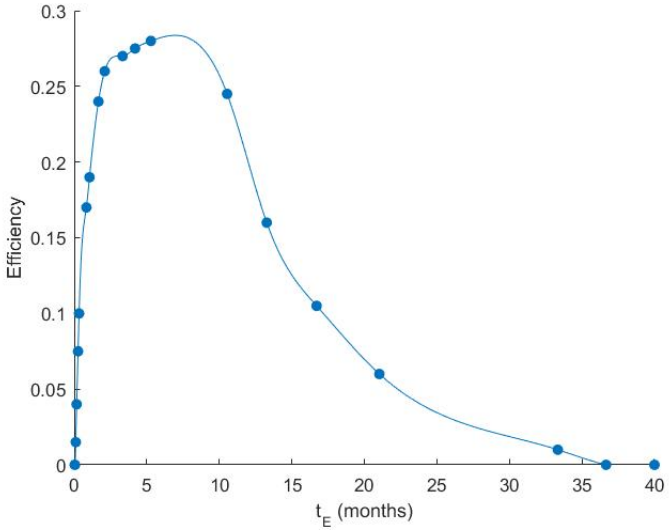


Figure 9: Efficiency of EROS2 towards LMC. Dots show the efficiency values and the curve is drawn using spline interpolation.

Following the same procedure as in the section 3.4, one can find the expected event rate $\Gamma$ by integrating the area under the histograms in the figures 10a to 10c. Table 2 shows the event rates corresponding to three masses after taking into account the efficiency.

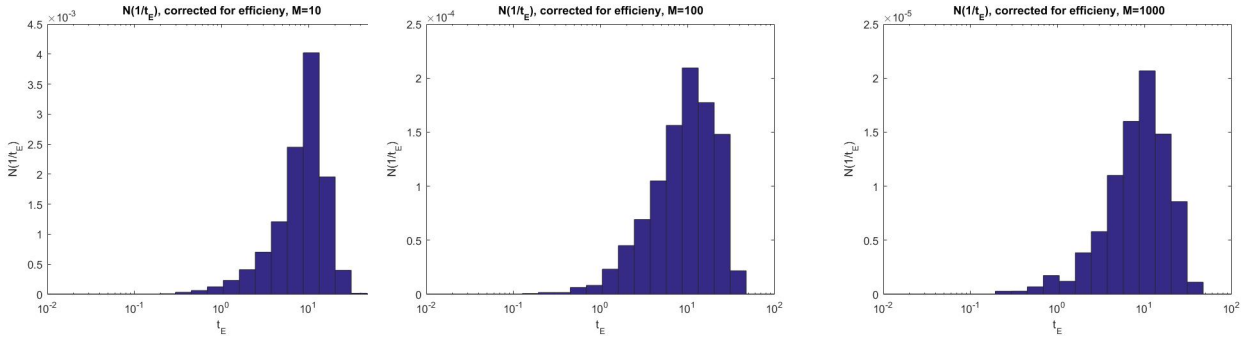


(a) (b) (c)

Figure 10: The corrected histograms after taking into account the efficiency $\epsilon(t_E)$

| Mass | $\Gamma$(event yr$^{-1}$ star$^{-1}$) |
|---|---|
| 10 $M_\odot$ | $8.88 \times 10^{-8}$ |
| 100 $M_\odot$ | $7.44 \times 10^{-9}$ |
| 1000 $M_\odot$ | $6.70 \times 10^{-10}$ |

Table 2: Event rate $\Gamma$ for three different masses after taking into account the efficiency of EROS2 survey towards LMC.

### 3.6 Number of expected events for EROS2

Now the number of expected events $N_{expected}$ can be estimated using the event rate:

$$N_{expected} = \Gamma \times T_{obs} \times N_{stars}, \tag{13}$$

where $T_{obs}$ is the duration of the experiment, and $N_{stars}$ is the number of monitored stars. Duration of EROS2 was approximately 6.5 years and the number of monitored stars towards LMC was roughly $N_{stars} = 3 \times 10^7$. The number of expected events for $10M_\odot$, $100M_\odot$ and $1000M_\odot$ are 17.3, 1.5 and 0.1 events, respectively.

## 4 Expectation from longer observations

So far we have considered the analysis of a single survey (EROS 2) towards the LMC. However, this target is (partially) monitored by many different surveys in the last 26 years. In the following, I estimate the number of expected events from combination of various surveys towards LMC.

### 4.1 Common field of view:

Equation 13 shows that the number of expected events depends on the number of stars monitored by a survey. To find the number of stars continuously monitored by different surveys, the common field of view between these surveys must be estimated. The fields of view of 6 different microlensing surveys are shown in the figure 11.

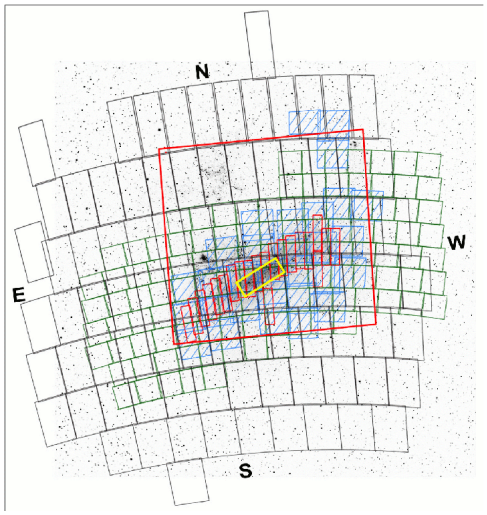


Figure 11: Positions of the monitored LMC fields. The red small rectangles and green squares show the OGLE-II and OGLE-III fields, respectively. The yellow rectangle and blue dashed squares show the CCD EROS 1 and MACHO fields, respectively. The large red square and the black rectangles show the EROS 1 and EROS 2 fields, respectively. OGLE-IV field (not shown here) overlaps all of these fields, except EROS 2 field (i.e., EROS 2 field does not completely overlap with OGLE-IV (figure from Moniez (2010)).

The size of the fields of view monitored by different microlensing surveys are shown in the the figure 12.

It is possible to estimate the common field of view between different surveys by finding the intersection of their field of views. Using the figure 11, we can distinguish the following three fields:

- Field 1: It is the common field of view between EROS 2, OGLE-III and OGLE-IV surveys. This field is monitored for 20 years and it covers about 35.6 deg$^2$ of the sky.
- Field 2: Common field between MACHO, EROS 2, OGLE-III and OGLE-IV surveys. It is monitored for 24 years (1992-2016) and it covers about 13.7 deg$^2$ of the sky.
- Field 3: Common field between EROS 1 CCD, MACHO, EROS 2, OGLE-III and OGLE-IV. The size of this field is about 0.44 deg$^2$ and it is monitored for more than 25 years.

In addition to the above field, the following fields are also useful in the analysis (see figure 15):

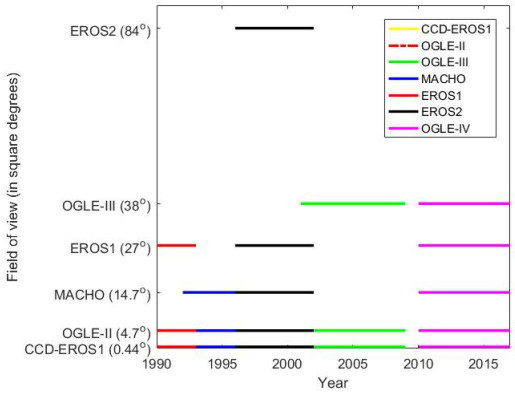


Figure 12: Timeline of microlensing surveys. For example, CCD EROS 1 field of view is monitored almost continuously by all the different microlensing surveys from 1990 to present days.

- Field $2'$: Complement of the field 2 with respect to the field 1.
- Field $3'$: Complement of the field 3 with respect to the field 2.

## 4.2 Number of common stars:

In this section , I estimate the number of stars in the fields 1, 2 and 3.

In the field 1, EROS 2 has the lowest limiting magnitude. So the stars observed in EROS 2 are also monitored by all other surveys in the field 1. The total area of the field covered by EROS 2 is 84 deg$^2$, and the total number of stars monitored in this field is $29.2 \times 10^6$. Hence, assuming a uniform distribution of stars in EROS 2 field, the number of stars in the field 1 (35.6 deg$^2$) is about $12.1 \times 10^6$. Since the distribution of stars in LMC is not uniform and the central region of LMC is more crowded, our approximation (based on uniform distribution) gives a lower limit value for the number of common stars.

Assuming a uniform distribution of stars in MACHO LMC field, one can estimate the number of stars in the field 2. About 93% of the MACHO field is inside OGLE-III field. There are about $1.19 \times 10^7$ stars in MACHO field. So the number of stars in MACHO field that are also monitored in EROS 2, OGLE-III and OGLE-IV surveys is roughly $1.11 \times 10^7$. Since the distribution of stars in MACHO field is not uniform, and the number density of the stars is higher at the center of the field, the true value of the number of stars in the field 1 could be higher than this value.

In the field 3, EROS 1 CCD is the smallest survey and it has the lowest limiting magnitude among all other surveys covering this field. Hence the number of stars that are covered continuously in this field is approximately equal to the number of stars covered by EROS 1 CCD ($10^5$ stars). The number of stars contained in each field together with the coverage duration are shown in the figure 13.

## 4.3 Number of expected events:

Number of expected events is given by:

$$N_{expected} = \int_{t_E} \Gamma \times N_{stars} \times T_{obs} \times \epsilon(t_E, T_{obs}) dt_E, \tag{14}$$

where $\Gamma$, $N_{stars}$, $T_{obs}$ and $\epsilon(t_E, \Delta T)$ are the event rate, number of stars in the field, duration of the survey, and detection efficiency (depending on the timescale of the event and duration of the observation), respectively. This equation is in principle same as the equation 13. The only difference is that the efficiency is explicitly present in this equation.

Longer observations will increase the detection efficiency for the long duration events. As a first approximation, the modified efficiency can be described by means of a simple scaling law:

$$\epsilon'(t_E) = \epsilon(\frac{\Delta T t_E}{\Delta T'}), \tag{15}$$

where $\Delta T$ is the duration of existing survey, and $\Delta T'$ is the duration of new survey with the efficiency of $\epsilon'(t_E)$. Figure 14 shows the dependence of detection efficiency on duration of the survey (with the scaling law).

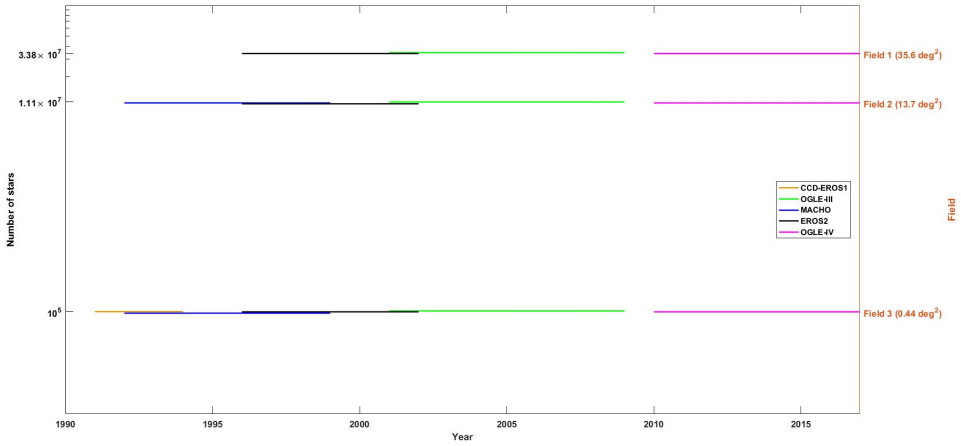


Figure 13: Approximate number of stars that are monitored in each of the fields.

## 4.4 Field 3

$10^5$ stars in the field 3 are monitored continuously for 26 years by all the surveys. The event rate and the number of expected events for three different masses are shown in the table 3.

| Mass | $\int \Gamma \epsilon(t_E, T_{obs}) dt_E$ | $N_{expected}$ |
|---|---|---|
| 10 $M_\odot$ | $0.68 \times 10^{-7}$ | 0.17 |
| 100 $M_\odot$ | $1.64 \times 10^{-8}$ | 0.04 |
| 1000 $M_\odot$ | $1.54 \times 10^{-9}$ | $3.85 \times 10^{-3}$ |

Table 3: Event rates $\Gamma$ and the number of expected events $N_{expected}$ for three different masses and for 25 years of observations of the field 3.

## 4.5 Field $3'$

The number of expected events in the field $3'$ is nothing but the difference between the number of expected events in the fields 2 and 3 (for 24 years of observations).

Detection efficiency is proportional to the length of the survey (i.e., longer observation gives better efficiency). We can use Eq. 14 with the new values of the detection efficiency to find the number of expected events in the field 2

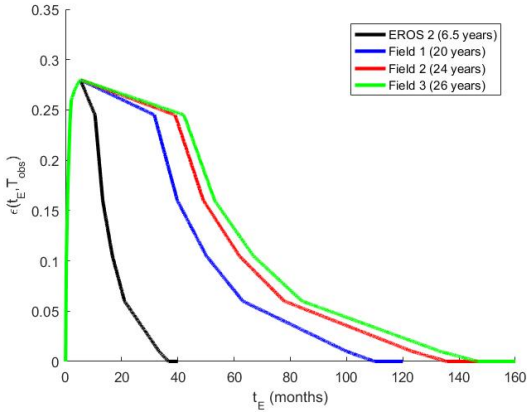


Figure 14: Detection efficiency increases with the duration of the survey. Using the known values of detection efficiency for EROS 2, and assuming a simple scaling law, the plot shows dependence of detection efficiency $\epsilon(t_E, T_{obs})$ on the timescale of the microlensing event $t_E$, and the duration of the survey $T_obs$.

($N_{stars} = 1.11 \times 10^7$) and the field 3 ($N_{stars} = 10^5$) with $T_{obs}$ =24 years. The results are shown in the table 4.

| Mass | $\Gamma$(event yr$^{-1}$ star$^{-1}$) | $N_{expected}$ (field 2) | $N_{expected}$ (field 3) |
|---|---|---|---|
| 10 $M_\odot$ | $1.36 \times 10^{-7}$ | 18.05 | 0.16 |
| 100 $M_\odot$ | $3.21 \times 10^{-8}$ | 4.26 | 0.04 |
| 1000 $M_\odot$ | $2.93 \times 10^{-9}$ | 0.39 | $3.51 \times 10^{-3}$ |

Table 4: Event rates $\Gamma$ and the number of expected events $N_{expected}$ for three different masses and for 24 years of observations of the fields 2 and 3.

Therefore, the number of expected events in the field 3′ for $10M_\odot$, $100M_\odot$ and $1000M_\odot$ are 17.89, 4.22 and 0.38, respectively.

### 4.6 Field 2′

Using the same logic as before, the number of expected events in the field 2′ is the difference between the number of expected events in the fields 1 and 2 (for 20 years of observations).

As it is mentioned before, the number of stars in the field 1 is about $1.21 \times 10^7$. Table 5 shows the event rates for 3 different masses for 20 years of observations, together with the number of expected events.

| Mass | $\Gamma$(event yr$^{-1}$ star$^{-1}$) | $N_{expected}$ (field 1) | $N_{expected}$ (field 2) |
|---|---|---|---|
| 10 $M_\odot$ | $1.34 \times 10^{-7}$ | 16.21 | 14.82 |
| 100 $M_\odot$ | $2.74 \times 10^{-8}$ | 3.31 | 3.03 |
| 1000 $M_\odot$ | $2.26 \times 10^{-9}$ | 0.27 | 0.25 |

Table 5: Event rates $\Gamma$ and the number of expected events $N_{expected}$ for three different masses and for 20 years of observations of the fields 1 and 2 (20 years of observations).

Hence, the number of expected events in the field 2′ for $10M_\odot$, $100M_\odot$ and $1000M_\odot$ are 1.39, 0.28 and 0.02, respectively.

### 4.7 Total Number of expected events:

Combined analysis of the fields 1, 2 and 3 gives the total number of expected events (figure 15):

$$N_{expected} = N_{expected}(3) + N_{expected}(3') + N_{expected}(2') \tag{16}$$

It is shown in the table 6

| Mass | $N_{expected}$ |
|---|---|
| 10 $M_\odot$ | 19.45 |
| 100 $M_\odot$ | 4.54 |
| 1000 $M_\odot$ | 0.40 |

Table 6: Total number of expected events $N_{expected}$ for three different masses and for 20 years of observations of the field 2′, 24 years of observations of the field 3′, and 25 years of observations of the field 3.

### 4.8 A remark about EROS 1 plate

If EROS 1- plate data is added to our database, we can define a new field (field 4) with a duration of 26 years. This field is the intersection between EROS 1- plate, EROS 2, MACHO, OGLE-III and OGLE-IV. In this case the total number of expected events for $10M_\odot$, $100M_\odot$, $1000M_\odot$ raise to 41.87, 11.42 and 0.97, respectively. However, since the quality of EROS 1- plate data is poor, it is not suitable for this purpose.

### 4.9 Conclusion

Combined analysis of different fields with different time of observations increases the number of expected events.

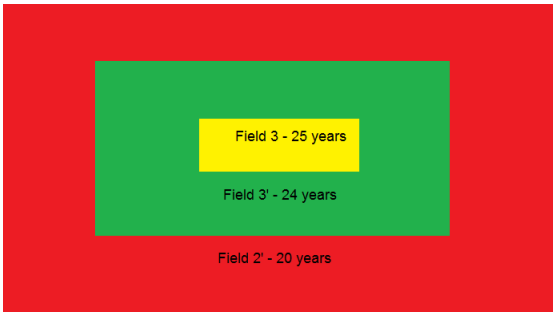


Figure 15: Three fields that are suitable for combined analysis.

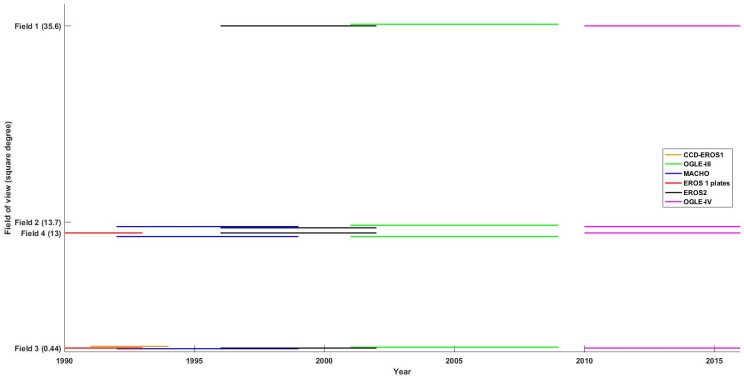


Figure 16: Combination of the fields including EROS 1 plate survey.

# 5 Data sources

In this section I describe the data sources that I used for constructing the light curves of variable stars in different surveys.

## 5.1 EROS 1 plate

The first phase of the EROS search for microlensing towards LMC was done between 1990 to 1993. 290 photographic plates were used in this survey at the ESO 1m Schmidt telescope, half with a blue filter and half with a red filter. As figure 11 shows, EROS 1 plate contains a single field towards LMC and about 4.2 million stars were monitored in this field.

For the analysis of the data, EROS 1 plate field is divided into 10 zones. Each zone has 80 tiles, except zone 10 which has 64 tiles (figure 17). A specific star in this database is identified by a set of two numbers: tile number and number of the star in the tile. I wrote a program in Python which takes the tile number and the number of the star in the tile, and then reads the photometric data of the star. Afterwards it constructs the light curves of the star in the blue and red bands.

## 5.2 MACHO survey

The MACHO project was a survey to search for dark matter in the form of massive compact halo objects. This survey was done between 1992 and 1999. Millions of stars in LMC, SMC and Galactic bulge were monitored to search for the microlensing events. In particular about 12 million stars were monitored in the LMC fields. Raw images and photometric data of MACHO survey are accessible online via *MACHO Project Data Service*[1]. A star in the MACHO database is identified by three numbers: field, tile and sequence. This set of three numbers is known as *star identifier*. The first number shows the MACHO field number which contains the star. Each field is divided into several tiles and in each tile there are sequences of stars. In order to access to the photometric data of a specific star, one has to follow the following three steps:

[1] http://macho.nci.org.au/

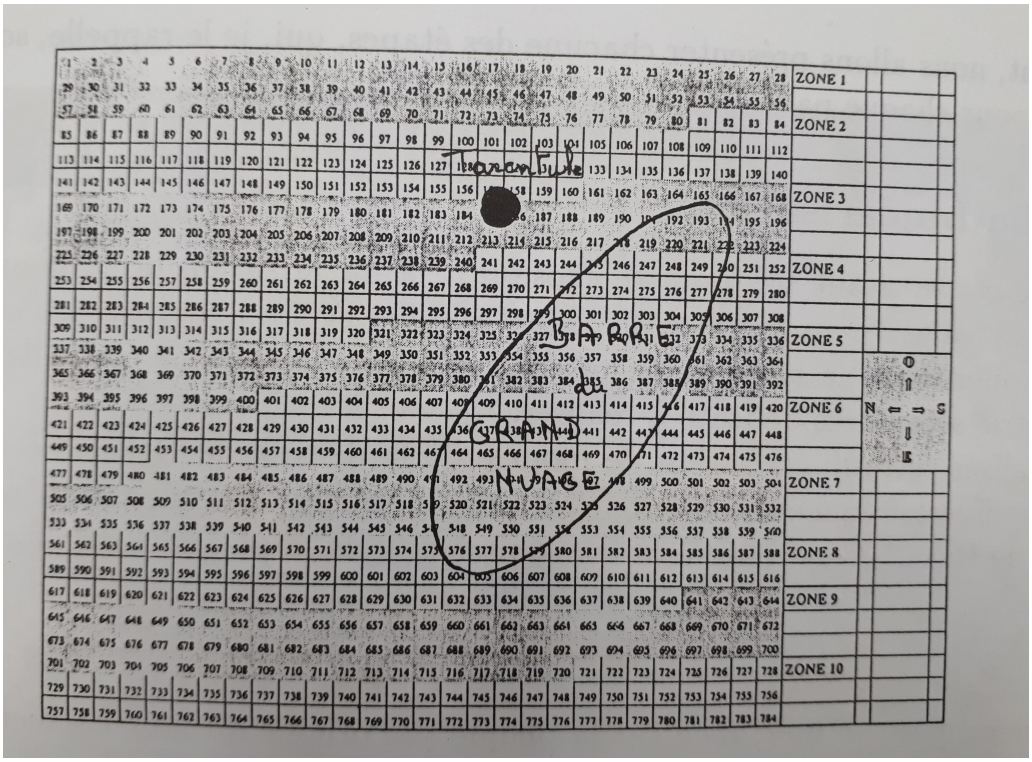


Figure 17: The EROS 1 plate field towards LMC. The field is divided into 10 zones and 784 tiles. Stars are numerated in each tile. Image from the thesis of Fabien Cavalier, 1994.

- The list of field center coordinates are available in the website. The first step is to determine the field number which contains the star.
- For each field there is a file (in CSV format) which contains the star identifier: field number, tile number and the star number (sequence), together with the coordinates of the star. One has to extract the star identifier of the desired star.
- After extraction of the star identifier, the photometry file of the corresponding tile must be downloaded. This file contains the set of all stars in that tile. Since the number of the star (sequence) is extracted in the previous step, it is possible to read the photometric data of the star.

### 5.3 OGLE survey

OGLE (**O**ptical **G**ravitational **L**ensing **E**xperiment) is a Polish microlensing experiment which is currently in the forth phase. The first phase of this experiment was done between 1992 to 1995 towards the Galactic bulge. In the second phase of OGLE (OGLE-II) the following three targets were monitored between 1996 to 2000: Galactic bulge, LMC and SMC. OGLE-III (started in 2001 and finished in 2009) monitored the same targets as OGLE-II; however the number of monitored stars in this phase was much larger than OGLE-II.

In this report I partially used the photometric data given by OGLE-III database. The photometric data of variable stars in OGLE-III are accessible online[2]. In this online database it is possible to find the counterpart of a variable star in MACHO database in OGLE-III survey by entering the *star identifier* of the MACHO object. Moreover, whenever the photometric data of OGLE-II is available for that object, the database gives the OGLE-II photometric data as well.

## 6 Connecting the light curves of different surveys

In order to search for the long duration microlensing events, we must be able to connect the light curves of millions of objects in the different surveys. To do so, a search for the object counterpart in various surveys must be performed in

[2]http://ogledb.astrouw.edu.pl/ ogle/CVS/

the first place. Then the x-axis (time) and y-axis (magnitude) of the light curve must be intercalibrated for different surveys. These are explained in the following subsections.

## 6.1 Nearest neighbour search and MACHO Light Curves

I would like to find the nearest neighbour of an EROS 1 plate object in the MACHO database. To find the nearest neighbours of an object in the sky, one can use the pseudo Pythagorean theorem. According to this theorem, the angular distance between two objects in the sky can be obtained by:

$$\cos\gamma = \sin\delta_a \sin\delta_b + \cos\delta_a \cos\delta_b \cos(\alpha_a - \alpha_b), \tag{17}$$

where $\gamma$ is the angular distance, and $(\alpha_{(a,b)}, \delta_{(a,b)})$ are the right ascension and declination of the two objects, respectively. By specifying the search radius ($\gamma$) around an object, one can find the nearest neighbour to that object. Nearest neighbour algorithm works as follows: First, it finds the nearest MACHO field to the position of the object in EROS 1 plate database. Then it looks for the neighbour stars within the specified search radius (7 arcsec by default) in that field and extract the identifier of those stars. The criterion for determining the counterpart of EROS 1 plate object in MACHO database is defined as follows:

If the nearest neighbour is within 0.5 arcsec and the distance to the next neighbour star is more than 5 arcsec, the nearest neighbour is identified as the counterpart of EROS object in MACHO database.

Afterwards, by means of the identifier of the nearest neighbour, it loads the corresponding photometry file and reads the photometric information of the nearest neighbour and constructs its light curve.

## 6.2 An example of nearest neighbour search algorithm

In the following a long period variable star in the EROS 1 plate catalog is chosen, its light curve is constructed and a nearest neighbour search is performed to find the counterpart of this object in MACHO database. Finally, the light curve of the counterpart of the object in MACHO database is plotted to check if it is the correct counterpart of EROS 1 plate object.

### 6.2.1 Time harmonization in EROS 1 plate light curve

In the EROS 1 plate database, the measurement times are computed as the number of days after the 31/12/1989 at 0h00. As we will see in the next part, MACHO measurement times are in terms of modified Julian date. Since our aim is to join the light curves of an object in EROS 1 plate and MACHO databases, we need to convert the EROS measurement times into the modified Julian date, so that the x-axis for the EROS 1 plate and MACHO be the same.

Julian date is the continuous count of days since the beginning of day starting at noon on January 1, 4713 BC. To convert calendar day (e.g. EROS measurement times) to Julian date the following formula can be used:

$$JD = 367Y - int(7(y + int((M+9)/12))/4) + int(275M/9) + D + 1721013.5 + UT/4, \tag{18}$$

where $JD, Y, M, D$ and $UT$ are Julian date, year, month, day and universal time, respectively. The symbol $int$ means that only the integer part of the argument inside the parentheses is considered. Now the modified Julian date ($MJD$) is defined as follows:

$$MJD = JD - 2400000.5. \tag{19}$$

After conversion of measurement times into the modified Julian dates, and reading the photometric data of an object, it is possible to construct the light curve of the star. I chose a long period variable star from the the catalog of EROS 1 plate variable stars. The light curve of this object is shown in the figure 18

### 6.2.2 Counterpart of the EROS 1 object in MACHO database

Now using the nearest neighbour algorithm, I can find the counterpart of EROS 1 object in MACHO database. This will result in the light curve shown in the figure 19. Comparing figures 18 and 19, it is evident that these two light curves correspond to the same object. Therefore we conclude that the nearest neighbour algorithm works correctly.

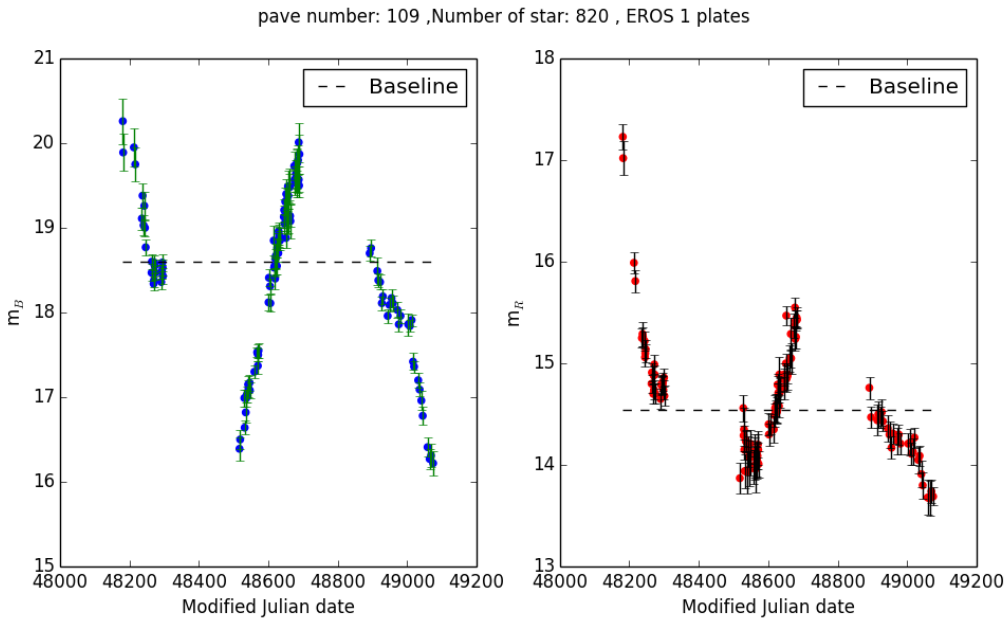


Figure 18: The light curve of a long period variable star in EROS 1 plate database in the blue (left) and red (right) bands. Y-axis shows the magnitudes of the object. The baseline shows the mode of magnitudes. The method of finding mode of the magnitudes is explained in the thesis of Nathalie Palanque-Delabrouille, 1997.

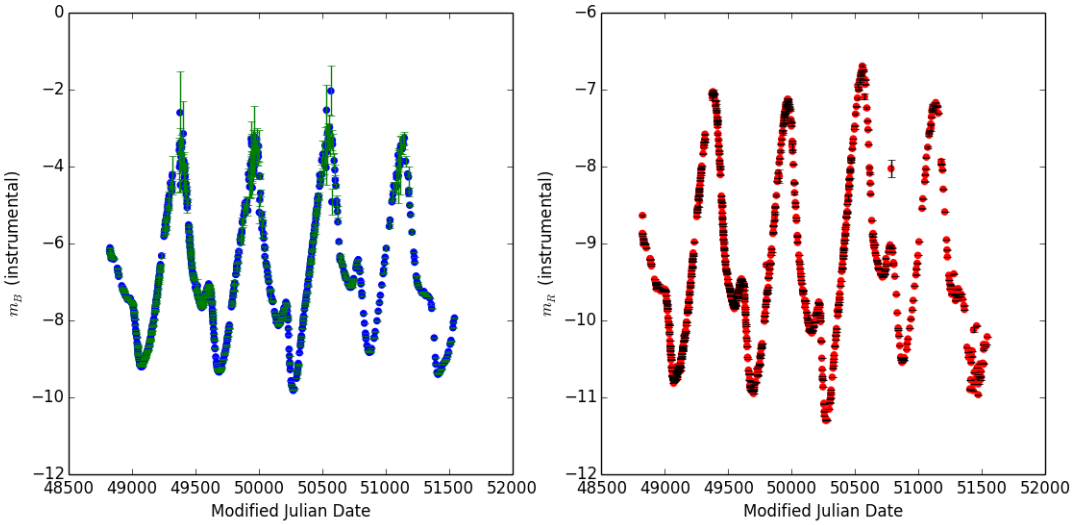


Figure 19: The light curve of the counterpart of EROS 1 plate object (figure **??**) in MACHO database. The $y$-axis shows the raw magnitudes of the object in the blue (right) and red (left) bands.

## 6.3 MACHO Photometry Calibration

In order to connect the light curves of MACHO and EROS 1 plate, one must transform the MACHO instrumental magnitudes to a standard system. The transformation is explained in detail by Alcock et al. 1999. In the following the calibration procedure is summarized. The transformation of the raw magnitudes into Kron-Cousins system is as follows:

$$V = V_{M,t} + a0 + (a1 + 0.022X_t)(V_{M,t} - R_{M,t}) + co + 2.5\log(ET), \tag{20}$$

$$R = R_{M,t} + b0 + (b1 + 0.004X_t)(V_{M,t} - R_{M,t}) + co + 2.5\log(ET), \tag{21}$$

where $V$ and $R$ are the calibrated magnitudes on the Kron-Cousins system, and $V_{M,t}$ and $R_{M,t}$ are the MACHO instrumental magnitudes in the blue and red bands, respectively. The exposure time ($ET$) of 300 seconds was used for observations of all LMC fields. *co* indicates chunk offset and $X_t$ is air mass of the template observation. There are four calibration coefficients in these equations: $a0, a1, b0$ and $b1$.

$a0$ and $b0$ are the zero-point calibration coefficients in blue and red, respectively. They are given by the following for all MACHO fields:

$$a0 = 18.410 - 0.279X_t, \tag{22}$$

$$b0 = 18.087 - 0.222X_t. \tag{23}$$

$a1$ and $b1$ are the color coefficients in blue and red, respectively. They depend on the CCD number used for the observation. Since CCD numbers are not available to determine $a1$ and $b1$, I used their mean values ($a1$=-0.2 and $b1$=0.1812).

In order to determine the chunk offset (*co* value), one needs *red west of pier chunk number* which is not explicitly given in MACHO database. However, chunk offset values that are given in Alcock et al. 1999, are of the order of 0.01 and can be neglected for the moment.

## 6.4 Combining Light curves

After the magnitude calibration of the object in MACHO, I try to combine the EROS 1 and MACHO light curves. I also add the OGLE data to the joint light curve. As it is mentioned in the section 5.3, OGLE-III online database provides the counterpart of variable stars in MACHO database. So, having MACHO identifier of the variable object, it is possible to find its light curve in OGLE-III database.

Measurement times of OGLE survey is in term of Heliocentric Julian Date (HJD). Heliocentric Julian date is the Julian date corrected for differences in Earth's position with respect to the sun. Since we have the MACHO and EROS 1 plate data in terms of modified Julian date, OGLE measurement times must be converted into the same unit of time. The relation between heliocentric Julian date and Julian date is as follows:

$$HJD = JD - \frac{r}{c} \cdot [\sin(\delta) \cdot \sin(\delta_\odot) + \cos(\delta) \cdot \cos(\delta\odot) \cdot (\cos(\alpha - \alpha_\odot)], \tag{24}$$

where $JD, r$ and $c$ are the Julian date, the heliocentric vector to the observe and speed of light, respectively. $\delta$ and $\alpha$ are the declination and right ascension of the object and the index $\odot$ indicates the position of the sun. For our purpose, the correction term is negligible with respect to the Julian date value and we can approximate the heliocentric Julian date by Julian date.

The joint light curves of two long period variable stars are shown in the figures 20 and 21. As it can be seen in the figures, apparent magnitudes are different in overlapping region between EROS 1 plate and MACHO data. The same happens in the overlapping region between MACHO and OGLE-II. This differences, which is due to the different filters used by different surveys, is potentially the most difficult problem for the search of microlensing event from a combination of different surveys.

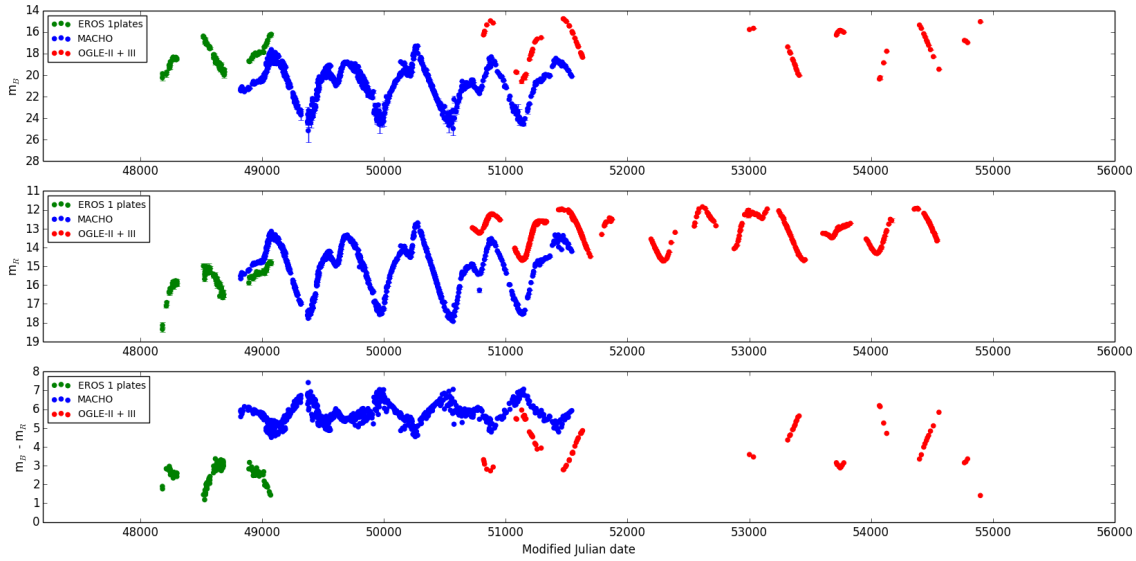


Figure 20: The joint light curve of a Mira variable star in blue (top) and red (middle) filters. The bottom panel shows the color difference B-R.

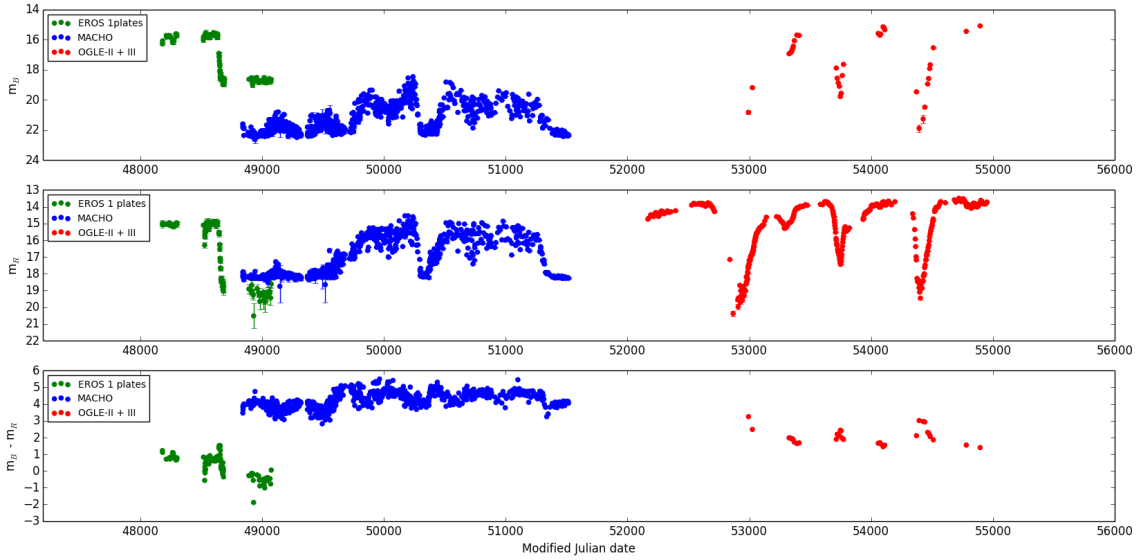


Figure 21: Joint light curve of another variable star in blue (top) and red (middle) filters. The color difference B-R is shown in the bottom panel. This star is classified as a R-CrB star in OGLE-III database. This type of stars are eruptive variables whose brightness changes in two modes, one low amplitude pulsation and one irregular sudden fading.

### 6.5 Connecting the light curves

The difference in magnitudes in overlapping regions in the figures 20 and 21 can be explained by the fact that different surveys are using different filters to record the magnitudes. One way to connect the magnitudes is to use the so called *color equations*. As an example, color equation takes the following form for connecting of B band magnitudes in EROS 1 plate to MACHO surveys (at the first order):

$$B_{EROS} = B_{MACHO} + a \times (B_{MACHO} - R_{MACHO}), \tag{25}$$

where $B_{EROS}$ and $B_{MACHO}$ are the B band magnitudes in EROS 1 plate and MACHO, respectively; $R_{MACHO}$ is the red band magnitude in MACHO, and $a$ is the color coefficient. A similar equation can be used to connect R band magnitudes:

$$R_{EROS} = R_{MACHO} + b \times (B_{MACHO} - R_{MACHO}), \tag{26}$$

where $R_{EROS}$ is the R band magnitude of the object in EROS 1 plate and $b$ is the color coefficient.

The way we establish the color equations is by using different photometric standard stars. These stars have a well-defined magnitude in a standard system and they can be used to transform the magnitudes of stars recorded by different filters into a standard system. The catalog of standard stars are available online.

## 7 Conclusion and perspectives

Since the efficiency of a combined survey gives a better sensitivity for very long duration events, the number of expected events from combination of several surveys is higher than that of a single survey. According to our extrapolated efficiency, we can expect to detect a few microlensing events of very massive objects with a few tens of solar masses or more.

In order to search for microlensing events due to very massive objects we need to connect the photometric data of the different surveys. However, since different surveys use different filters the connection of light curves is not straightforward. The solution for connecting the apparent magnitudes in different systems is by establishing the color equations from a large number of stable stars using the catalog of standard stars with standard photometric data. I will work on this issue in the rest of the internship.

## References


Alcock, C., Allsman, R. A., Alves, D., et al. 1997, ApJ, 486, 697

Alcock, C., Allsman, R. A., Alves, D. R., et al. 1999, PASP, 111, 1539

Ansari. R., Cavalier, F., Moniez, M., et al. 1996, A&A, 314, 94

Cavalier F., 1994, PhD thesis

Moniez M., 2010, General Relativity and Gravitation, 42, 2047

Palanque-Delabrouille N., 1997, PhD thesis